



HAL
open science

Dynamic remodeling of the dynamin helix during membrane constriction

Adai Colom, Lorena Redondo-Morata, Nicolas Chiaruttini, Aurelien Roux,
Simon Scheuring

► **To cite this version:**

Adai Colom, Lorena Redondo-Morata, Nicolas Chiaruttini, Aurelien Roux, Simon Scheuring. Dynamic remodeling of the dynamin helix during membrane constriction. *Proceedings of the National Academy of Sciences of the United States of America*, 2017, 114 (21), pp.5449 - 5454. 10.1073/pnas.1619578114 . inserm-01653772

HAL Id: inserm-01653772

<https://inserm.hal.science/inserm-01653772>

Submitted on 1 Dec 2017

HAL is a multi-disciplinary open access archive for the deposit and dissemination of scientific research documents, whether they are published or not. The documents may come from teaching and research institutions in France or abroad, or from public or private research centers.

L'archive ouverte pluridisciplinaire **HAL**, est destinée au dépôt et à la diffusion de documents scientifiques de niveau recherche, publiés ou non, émanant des établissements d'enseignement et de recherche français ou étrangers, des laboratoires publics ou privés.

Abstract:

Dynamin is a dimeric GTPase that assembles into a helix around the neck of endocytic buds. Upon GTP-hydrolysis, dynamin breaks these necks (1), a reaction called membrane fission. Fission requires dynamin to first constrict the membrane (2-4). It is unclear however, how dynamin helix constriction works. Here we undertook a direct high-speed atomic force microscopy imaging analysis to visualize the constriction of single dynamin-coated membrane tubules. We show GTP-induced dynamic rearrangements of the dynamin helix-turns: the average distances between turns and between dimers along the polymer reduce with GTP-hydrolysis. However, these distances vary over time, as helical turns were observed to transiently pair and dissociate. At fission sites, these cycles of association and dissociation were correlated with relative displacement of the turns and constriction. Our findings support a model in which conformational changes at the dimer level drive relative sliding of helical turns, and constriction by torsion.

Significance Statement

The GTPase dynamin catalyzes membrane fission and is essential in endocytosis and other events such as organelle division. Dynamin is a unique molecular motor with torsional and contractile abilities. Because these abilities involve a conformational change at the whole polymer level, standard structural biology tools have not been able to fully unravel the mechanism by which it constricts and twists. Here, we used high-speed atomic force microscopy to image the constriction and fission of dynamin-coated tubules with sub-nanometer and sub-second resolution. Our results provide important findings to establish the contribution of the various constriction mechanisms.

\body

Results:

In absence of nucleotides, the molecular structure of the dynamin-1 dimer (5, 6) and dynamin-3 tetramer (7) revealed that dynamins are composed of a rigid stalk, connecting the membrane-binding Pleckstrin Homology (PH) domain to the GTPase domain (see **Fig. 1a**). In the dimer, the stalks form a cross, with the GTPase domains on one side, and the PH domains on the other. This architecture allows membrane binding through a specific interaction between the PH domains and phosphoinositide(4,5)bisphosphate (PIP₂). The GTPase domain is connected to the stalk via a flexible hinge called BSE (Bundle Signaling Element) (8, 9). The crystal structures also provided evidence how molecular interactions between dimers lead to the formation of a helical polymer (5-7). In particular, in the tetrameric form (7), GTPase domains from two contiguous dynamin dimers are closely apposed, forming a structural dimer identifiable in the helical structure (see blue-orange dimer in **Fig. 1a**). In the

65 following, we will call this dimer “helical dimer”, as it is not equivalent to the
66 biochemically stable dimer (see Fig. 1a).

67 Also, helical dimers from adjacent turns in the helix are closely apposed, suggesting that
68 they may participate in molecular links between turns (see Fig. 1a). Cryo-EM 3D-
69 reconstructions of dynamin helices were compatible with these models (10), even
70 though the number of dimers per helical turn varied from 14 to 18 (7). Cryo-EM
71 reconstructions of the dynamin helix in the presence of GMP-PCP, a non-hydrolysable
72 GTP-analog, revealed a more constricted state with 13 to 15 dimers per turn (10-12).
73 Altogether, X-ray and cryo-EM studies have shown that dynamin dimers undergo a
74 conformational change leading to the constriction of the membrane tubule beneath (4,
75 10-13). Among these reconstructions the internal organization of dynamin domains is
76 dramatically different: each dimer undergoes a slight rotation along the axis
77 perpendicular to the membrane (called the “cork-screw” model in (12)), and a change of
78 the GTPase domain positions (see Fig. 1a, conformational change in the “helix
79 compaction” model). Such conformational change leads to a compaction of the polymer
80 that could constrict the membrane (12)(see Fig. 1a, helix compaction). In this model, the
81 relative position of helical dimers in adjacent turns does not change during constriction
82 (see blue-yellow dimers in Fig. 1a), and molecular links between adjacent turns are
83 conserved.

84 However, a super-constricted state was recently obtained with GTP and the GTPase-
85 reduced mutant dynamin K44A (4). This structure had 11 dimers per turn, suggesting
86 that relative sliding of adjacent turns occurred during constriction. If the helix constricts
87 by torsion, the relative positions of helical dimers in adjacent turns change dramatically
88 upon constriction (see Fig. 1a, helix torsion). Supporting this model, optical microscopy
89 of long dynamin-coated membrane tubules showed twisting upon GTP-hydrolysis,
90 suggesting that constriction was accompanied by torsion of the entire helix (14, 15).

91 In the torsion model however, transient breakage of molecular links between helix
92 turns is required to allow for sliding and torsion. GTPase domains, which participate in
93 molecular links between adjacent turns, would thus have to undergo cycles of
94 dissociation/association coupled to their GTPase cycle. Crystal structures are
95 compatible with this hypothesis: no links between GTPase domains are found in absence
96 of nucleotide (5-7). But a truncated dynamin has been crystalized with GDP·AlF₄⁻ (8), a
97 nucleotide mimicking the hydrolytic state of GTP in dynamin, and in this state, GTPase
98 domains interact strongly (termed ‘G-G link’ in the following). Also the BSE moves by an
99 angle of approximately 70° relative to the nucleotide-free structure, suggesting that the
100 GTPase domains generate a powerstroke driving turn sliding and torsion upon GTP-
101 hydrolysis (13).

102 While torsion and compaction are not exclusive, as both mechanisms could occur at
103 the same time in constriction, we ought to test the torsion model by visualizing the
104 global conformational changes of single dynamin-coated membrane tubules with
105 molecular and sub-second resolutions: we adapted *in vitro* reconstitution assays for
106 high-speed atomic force microscopy (HS-AFM (16)) that has recently proven powerful
107 for the study of membrane remodeling proteins on mica-supported bilayers (17). We

108 found that the adhesion of the proteins to the mica could impair the dynamin helix
109 conformational change. To overcome this technical limitation, we coated the mica with
110 biotin-lipid bilayers and attached partially (10%) biotinylated dynamin tubules via
111 streptavidin. We reasoned that one tenth of the dynamins being biotinylated, we would
112 have in average about one functionalized dynamin per helix turn, and hence anchorage
113 of the tubules to the support about every ten turns. This strategy generates links strong
114 enough to avoid displacement of the tubules during HS-AFM scanning, but spreads
115 attachment points far enough for providing motional freedom (18) and allowing to
116 observe conformational changes of the dynamin-helix (**see Methods for details**).

117 First experiments were performed with 100% di-oleyl-phosphatidylserine (DOPS)
118 liposomes (2) mixed with Δ PRD (deleted-Proline-Rich-domain) human dynamin-1
119 expressed and purified from bacteria (5). 100% DOPS was used as it favored the
120 formation of long dynamin-coated tubules in electron microscopy assays (2, 3). We
121 confirmed that Δ PRD-dynamin bound to DOPS liposomes and deformed them into long
122 membrane tubules decorated by a dynamin helix (**Fig. 1b-c**), as previously observed (2,
123 19). Δ PRD-dynamin was used instead of full-length dynamin because absence of the
124 flexible PRD-domain resulted in better resolution in HS-AFM images (see **Fig. S1a,b**).
125 The average thickness of these tubules was 63.0 ± 10.4 nm ($N = 28$) (mean \pm SD, as
126 throughout the article, unless noted) and the pitch of the striations was 19.2 ± 3.6 nm
127 ($N = 141$ turns on 4 tubules, see **Fig. 1c**). We measured similar values in EM images
128 (diameter: 59.0 ± 4.5 nm; $N = 26$, pitch: 15.0 ± 4.5 nm, $N = 38$ tubules), consistent with
129 previous reports (2). It is noteworthy that HS-AFM contours only the protein surface,
130 which in the case of dynamin is composed of helical dimers. Whenever we refer in the
131 following to dimers, we examine the structure and position of these surface exposed
132 domains – helical dimers – and cannot provide information about intramolecular
133 conformational changes.

134 We then added 10 μ l of a 10mM GTP-solution to the 90 μ l fluid chamber volume,
135 resulting in 1.1mM GTP. Right after GTP-addition, we often observed tubules
136 constriction (see **Fig. 1b-d, Movie S1, Fig. S1c-h**). Constriction, however, appeared very
137 inhomogeneous, with some parts remaining unconstricted and others narrowed. This
138 constriction was not due to forces applied by the AFM tip onto the tubule, as the same
139 constriction was visible on other tubules when the field of observation was widened
140 (compare **Fig. 1b** with **Fig. 1d, Fig. S1c** with **S1e, Fig. S1g** with **S1h**). As well, the
141 constriction was also observed in the more physiological conditions in which full-length
142 dynamin was used to generate tubules out of liposomes formed of brain extract lipids
143 supplemented with 15% PIP₂ (**Fig. S1i**). The dynamin-coat remained mostly attached,
144 and striations were visible during the constriction of the tubules, even though the
145 regularity of the pattern was strongly affected (**Fig. 1c, Fig. S1d, f**). At some of the most
146 constricted locations, the tubule was virtually invisible, suggesting that fission may have
147 occurred at these sites (**Fig. 1c and Fig. S1**, orange arrowheads).

148 In order to achieve higher temporal resolution imaging of the constriction, we
149 acquired HS-AFM movies at 0.96s/frame (**Fig. 2a, Movie S2**) and 1.5s/frame (**Fig. 2b,**
150 **Movie S3**). When GTP was added to the observation chamber, a slow constriction of the

151 dynamin-coated tubules was observed (see **Fig. 2a-c**, **Fig. 2f-g**, **Fig. S2a-c**). Such
152 continuous constriction of tubules was never observed in the absence of GTP (**Fig. 2h**)
153 or after addition of GDP·AlF₄⁻ (**Fig. S3a-c**). A minor, homogenous constriction was
154 observed in the presence GMP-PCP (**Fig. S3d-h**), consistent with the cryo-EM data that
155 showed a more constricted state when ΔPRD-dynamin was loaded with GMP-PCP (10,
156 11).

157 Upon GTP-addition, the initial tubule thickness of 60-70 nm reduced to 20-30 nm in
158 the most constricted sites (**Fig. 2f-g**, **Fig. S2a-c**). As compared to previous estimates of
159 the constriction dynamics of 0.5-1 s (15), the slow constriction dynamics observed in
160 these movies is most probably due to friction with the surface and steric hindrance
161 caused by the streptavidin/biotin bonds, as some tubules showed faster constriction
162 upon a single GTP-addition (e.g. **Fig. 1c**). However, these movies have lower resolution,
163 which suggests that these tubules have fewer bonds with the surface, being freer to
164 move. But the continuous, slow constriction observed (**Fig. 2a-b**, **Movies S2-3**) argues
165 for an active process triggered by multiple cycles of GTP-hydrolysis, rather than an
166 abrupt, single-event conformational change.

167 After the slow progressive constriction of the entire tubule, a more rapid reduction
168 of the tubule thickness at the most constricted locations was observed (see between
169 time 40 and 50 min in **Fig. 2f**). However, the HS-AFM tip still recorded a height of about
170 18-23 nm in these locations (**Fig. 2g**). This could be explained by highly curved but not
171 broken membrane tubules, or remains of the dynamin coat attached to streptavidin onto
172 the supported bilayer after fission. The height of the dynamin/streptavidin/lipid
173 complex generated for anchoring the tubules to the mica surface is in the range of 15-
174 20 nm (**Fig. S4**). We thus concluded that fission had occurred and that the remaining
175 measured height corresponded to remnants of the dynamin coat at the fission site still
176 linked to the supported bilayer on the mica.

177 Interestingly, in some constricted parts of the tubule, the resolution was high enough to
178 resolve the helical turns of dynamin (**Fig. 2d**, **Fig. S2d**; **Fig. S2e**). Our observations show
179 that fission occurred where the helical turns are the most constricted (**Fig. 2d**, **Fig. S2d**).
180 Due to limitations of how far the tip can penetrate between dynamin turns, it is not
181 detectable in these images whether partial disassembly occurred at the fission site or
182 not. It is however clear that highly constricted turns are in close vicinity to the fission
183 site, and that the depth within the fission site is significantly deeper than the one of the
184 surrounding constricted turns (**Fig. 2d**, end of kymograph). Thus, fission clearly
185 occurred where the curvature gradient along the tubule axis was highest, as previously
186 proposed (20).

187 During constriction of the tubule, the helical pattern remained visible most of the time
188 (**Fig. 2d**, **Fig. S2d**). Interestingly, some of the helical turns moved apart, some seemed to
189 collapse into a single turn and/or split upon GTP addition, which we interpret as pairing
190 and dissociation of neighboring turns (arrows in **Fig. 2a and d**, see also **Fig. 4a**).
191 Moreover, the 'intensity', i.e. the height of the turns, greatly varied with time, as
192 expected during constriction. On the contrary, neither lateral rearrangements nor height
193 variations were observed in the absence of GTP (**Fig. 2e**), nor in the presence of GMP-

194 PCP or GDP·AlF₄⁻. Importantly, these variations and rearrangements are unrelated to
195 fluxes occurring in the chamber upon GTP addition, as they did not occur upon buffer
196 addition. We quantified these rearrangements: On average, the helix pitch reduced from
197 19.2 ± 3.6 nm ($N = 141$) to 15.2 ± 4.9 nm ($N = 38$) (**Fig. 2i**), consistent with the helix
198 height profile showing closer turns (**Fig. 2j**), yet the standard deviation, *i.e.* the
199 variability of the pitch, increased. Along with this helix shortening, we observed a
200 significant change of turn lateral thickness (see blue arrows in **Fig. 2d**). This could be
201 due to turn pairing, as described above, or to a change of the angles between turns and
202 the tubule axis: from a sharp distribution around 90°-95° in absence of GTP, the angles
203 spread from 50° to 105° with GTP (**Fig. 2k**). This change of orientation was highly
204 dynamic (**Fig. 2a**, orange arrow, **Fig. S2e**). Altogether, our results show that GTP-
205 hydrolysis changes a rather regular helix into a highly dynamic and variable structure
206 on the way to fission, a behavior that could not be pictured by the previous static,
207 averaged structures of crystallographic and cryo-EM data.

208 The resolution of the images on DOPS tubules was however insufficient to visualize
209 the details of the helical reorganization process at the single protein level, most
210 probably because DOPS tubules have a low rigidity limiting HS-AFM resolution (16, 21).
211 To improve HS-AFM contouring and thus the resolution of the images, we opted for the
212 use of rigid lipid nanorods formed by the spontaneous assembly of galactocerebrosides
213 (22, 23). Galactocerebrosides were supplemented with 5% PIP₂ to mediate dynamin
214 binding to the nanorods (22). Nanorods are rigid and cannot be constricted by dynamin.
215 Indeed, once assembled onto these templates in absence of GTP (**Movie S4**),
216 substructures of the helix were resolved (**Fig. 3a**): the pitch of the helix was
217 15.4 ± 2.9 nm (**Fig. 3b**) similar to previous estimates (2, 3, 10, 22), a bit shorter than on
218 the DOPS tubules (**Fig. 2i**). Along the helical path, we observed rigid bodies (**Figs. 3a** and
219 **4a**) that we interpreted as helical dimers, spaced by 12.7 ± 2.3 nm. Moreover, molecular
220 links bridging adjacent turns at the position of each rigid body, of the helix were clearly
221 resolved (**Fig. 3a**, arrow). We interpreted these links as G-G links, between adjacent
222 helical dimers (8).

223 We then added GTP to these dynamin-coated nanorods during HS-AFM imaging. We
224 never observed constriction, however, strong modifications of the dynamin helix
225 occurred. On average, the pitch of the helix shortened by about 30% upon GTP-addition
226 (**Fig. 3b**). But the well-preserved periodicity of the helix in absence of GTP, was lost
227 upon GTP-addition: in some cases, we observed a shortening of the peak-to-peak
228 distance in the helix height profile (**Fig. 3c**, **Movie S5**) similar to what was seen on DOPS
229 tubules (**Fig. 2i**). In other cases, height profiles showed increasing distances between
230 peaks after GTP-addition (**Fig. 3d**, **Movie S6**), consistently with a previous report that
231 the helix pitch was larger after GTP-hydrolysis on nanorods (22). To explain this
232 variability within our observations, we checked by negative stain EM how dynamin-
233 coated nanorods behaved upon GTP-treatment. As previously reported (22), we
234 observed helices with increased pitch distance (**Fig. S5a,b**), but we also found
235 compacted helices with a shorter pitch (**Fig. S5c**), consistent with the pitch reduction
236 observed by HS-AFM (**Fig. 3b, c**).

237 Altogether, these observations show strong dynamics of dynamin helical turns during
238 GTP-hydrolysis. Indeed, we were able to observe adjacent turns undergoing dynamic
239 cycles of association/dissociation in presence of GTP (**Fig. 4a**), but we cannot provide
240 statistics whether more than two neighboring turns can be clustered by such pairing.
241 These observations are consistent with the pairwise collapse and separation of helical
242 turns observed on DOPS tubules (**Fig. 2d**). This dynamical breathing of the dynamin
243 helix turns suggests that the G-G-links can be either tighter, causing the apparent pairing
244 of two adjacent turns, or looser, causing turns to separate, in the presence of GTP
245 (**Fig. 4a**, white arrows). However, we cannot exclude that these cycles of
246 association/dissociation are not random collisions, as we could not observe molecular
247 links between helical dimers in all experiments.

248 Our results on the dynamic changes observed in the pitch and angle of helical turns
249 show that the constriction observed on membrane tubules is correlated with processive
250 cycles of helical turns pairing and separating, probably consecutive to conformational
251 changes at the level of each dimer. Importantly, the dynamical breathing of dynamin
252 turns described above is an essential postulate of the torsion model (see **Fig. 1a**): this
253 model implies that dynamins in neighboring turns must dissociate to allow constriction,
254 slide and reassociate to perform constriction.

255
256 However, we also noticed that the distances between helical dimers along the helical
257 path reduced upon GTP-addition (**Fig. S5d**). The distribution of these distances changed
258 from a single peak distribution centered on 12-14 nm in absence of GTP to a
259 heterogeneous distance distribution with two apparent peaks in presence of GTP, one
260 around 6-10 nm and the other remaining at 12-14 nm (**Fig. S5d**). This change of
261 distances could be the result of GTPase domains powerstroke upon GTP hydrolysis, as in
262 the torsion model GTPases domains have been proposed to slide turns relatively
263 through a myosin-like mechanism (24). But this change of distances could also be the
264 result of a helix compaction following a cork-screw intramolecular conformational
265 change (see **Fig. 1a** and (12)). We thus looked for further evidence of relative
266 displacement of adjacent helical turns.

267 As nanorods do not allow constriction, we looked for evidences of turn relative
268 displacement on DOPS tubules. Although DOPS tubules are softer than nanorods,
269 occasionally helical dimers were visible (**Fig. 2b**, fission point 1 (F.P.1), at higher
270 magnification in **Fig. 4b**) in particular when the tube was already highly constricted and
271 therefore probably more rigid. Close to fission sites, the evenly spaced helical dimers
272 moved with respect to each other in adjacent turns (**Fig. 4b**): While the topographic
273 heights – interpreted as helical dimers – are basically aligned facing each other at
274 $t=0\text{min}03\text{s}$ (**Fig. 4b**, red and blue outlines), the same are later ($t=156\text{s}$) in a clearly non-
275 aligned zig-zag arrangement. Also, the profiles show that these lateral movements are
276 associated with a reduction of the height of the turns, and thus with constriction
277 (**Fig. 4b**, profiles). These results evidence the relative displacement of helical dimers
278 from neighboring turns, but does not clearly show relative sliding of turns over a
279 distance larger than the size of a helical dimer.

280 To provide further evidence for this lateral sliding, we undertook another approach:
281 We ought to visualize dynamin oligomer displacements on the surface of a supported
282 lipid bilayer. We noticed however that Δ PRD-dynamin hardly formed oligomers at the
283 surface of mica-supported bilayers (**Fig. S6a**), most probably, because the substrate is
284 too rigid to allow for a minimal bending of the membrane required for dynamin
285 oligomerization. To overcome this problem, we thought of using two stacked
286 membranes instead of one, expecting the top membrane to be more deformable. The
287 first layer was generated by vesicle-fusion of positively charged GUVs (containing
288 DOTAP) onto the mica, onto which we added negatively charged GUVs (containing
289 DOPS). As expected, Δ PRD-dynamin bound specifically to negatively charged lipids
290 (**Fig. S6b**). Indeed, negative stain EM of these dynamin-coated surfaces showed a
291 striking assembly of short disordered dynamin oligomers (**Fig. 4d**). GTP-treatment
292 produced an increase of the fluorescence signal in absence of soluble dynamin (**Fig. S6b**,
293 panel +GTP). This increased fluorescence signal could be related to clustering of short
294 oligomers. In agreement, EM showed aggregation of oligomers after GTP-addition
295 (**Fig. 4c**, panel +GTP). Further support for this came from AFM nanomechanical
296 measurements (**Fig. S6c and e**), that showed an increased rigidity from
297 59 MPa \pm 18 MPa to 130 MPa \pm 43 MPa of the dynamin-coated membrane after GTP-
298 addition, consistent with the formation of clustered dynamin structures on the
299 membrane.

300 We then studied the dynamics of dynamin oligomers on these double-stacked
301 supported bilayers upon GTP-addition using HS-AFM (**Fig. S6d,e**). Even though we could
302 not resolved single dynamin oligomers, we observed displacements of elongated
303 structures from large protein domains (**Fig. 4d**, **Fig. S7a,b**, **Movies S7,8**). We
304 interpreted these movements as resulting from the sliding of the short dynamin
305 oligomers relative to each other. The movements of the dynamin chains could change
306 direction over time (**Fig. 4d**, kymograph). These observations are in further support that
307 GTP may lead to relative lateral displacement between adjacent dynamin oligomers.

308 Our study shows that GTP-hydrolysis induces striking changes in the helical
309 structure of assembled dynamin: First, adjacent helix turns can transiently dissociate
310 and reassociate, probably through transient unbinding of G-G links. Second, the helix
311 constricts concomitantly with these molecular rearrangements. However, this
312 constriction is not homogeneous, which may be linked to the difficulty of propagating
313 the constriction along the length of long helices (15). Third, fission occurs where
314 constriction is the strongest, consistent with previous findings (20). Also, we did not
315 observe any detectable disassembly of the dynamin coat upon GTP-hydrolysis, which
316 may question that disassembly is an important step of the fission reaction (24). Our
317 results are thus in support of a model where the GTPase domains transiently interact to
318 induce a powerstroke upon GTP-hydrolysis, driving turn sliding and constriction
319 through torsion (25, 26). However, our study of the dynamics of the topographic surface
320 of dynamin tubules does not provide any information about internal rearrangements of
321 the dynamin coat, leaving entirely open the possibility that this torsion is accompanied
322 by a compaction of the polymer.

323 **Materials and methods:**324 **Lipid suspensions**

325 All lipids were purchased from Avanti Polar Lipids, the galactocerebrosides from Sigma.

326

327 **Large Unilamellar Vesicles (LUVs).** Vesicles were prepared using 100% 1,2-dioleoyl-
 328 *sn*-glycero-3-phospho-L-serine (DOPS) or DOPS:1,2-dioleoyl-*sn*-glycero-3-
 329 phosphoethanolamine-N-(cap biotinyl) (Biotinyl Cap PE) 90:10, mol:mol, mixture or 1,2-
 330 dipalmitoyl-*sn*-glycero-3-phosphocholine (DPPC):Biotinyl Cap PE 90:10, mol:mol,
 331 mixture. Lipids dissolved in chloroform were dried under N₂ flux, followed by 30'
 332 incubation in a vacuum oven at 30°C or 2h in a desiccator. Hereafter, lipids were fully
 333 rehydrated with GTPase buffer (20 mM HEPES, 150 mM NaCl, 5 mM MgCl₂ at pH 7.4) for
 334 10 min at RT, obtaining a 2.5 mg/ml lipid solution. Finally, the lipid suspension was
 335 vortexed for 10 s and freeze-thawed three times in liquid nitrogen and a water bath,
 336 respectively.

337

338 **Nanorods.** The lipid composition of the nanorods is: galactocerebrosides:L- α -
 339 phosphatidylcholine (Egg PC):L- α -phosphatidylinositol-4,5-bisphosphate
 340 (PI(4,5)P₂):cholesterol:Biotinyl Cap PE 40:40:10:9:1 mole ratios. The nanorod lipid mix
 341 was dried under N₂ flux, followed by 30 min under vacuum at 30°C (Thermo Scientific
 342 Heraeus) or 2h in a desiccator to allow completely solvent evaporation. After, GTPase
 343 buffer was added to rehydrate the lipids for 10 min at RT to a final concentration of
 344 2.5mg/ml. The mixture was vortexed for 10 s and sonicated for 10 min in a bath
 345 sonicator. In the end, a tip sonicator (Active Motif) was applied to the solution during 2 s
 346 at 60W and 20kHz.

347

348 **Giant Unilamellar Vesicles (GUVs).** Giant Unilamellar Vesicles (GUVs) were composed
 349 of 100% DOPS or 100% 1,2-dioleoyl-3-trimethylammonium-propane (DOTAP). GUVs
 350 were prepared by electroformation. Briefly, 20 μ L of 1 mg/mL lipid solution were
 351 deposited on two indium tin oxide (ITO)-coated glass slides (70-100 Ω surface
 352 resistivity, from Sigma) and vacuum dried. A \sim 1 mm thick O-ring was used as spacer to
 353 form a chamber between the two ITO slides, which was filled with 200 mM sucrose and
 354 exposed to 1V AC-current with a 10 Hz sinusoidal wave for 1 h. The resulting GUVs
 355 suspension was carefully harvested and used within the same day.

356 **Dynamin-coated lipids preparation.** For the lipid tubulation with dynamin, 5 μ l of
 357 LUVs suspension were mixed with 2 μ l (0.9 mg/ml) of Δ PRD-dynamin (containing 10%
 358 of biotinylated- Δ PRD-dynamin) and 10 μ l of GTPase buffer during 30 min at RT. For the
 359 dynamin-coated nanorods, 5 μ l of nanorods suspension were used for the reaction
 360 instead.

361 **Supported lipid bilayers.** For mica-Supported Lipid Bilayers (SLBs), LUVs composed of
 362 DPPC:Biotinyl Cap PE 90:10, mol:mol, were deposited onto freshly cleaved mica,
 363 incubated for 15 min and rinsed thoroughly with GTPase buffer. For the formation of

364 two-stacked SLBs, the sample was prepared by first depositing DOTAP GUVs on a freshly
 365 cleaved mica disk. After the Supported Lipid Bilayer was formed, the sample was
 366 carefully rinsed with GTPase buffer. Then, DOPS GUVs were deposited, forming a double
 367 bilayer, the closest to the mica being the DOTAP bilayer and the farthest the DOPS
 368 bilayer. After rinsing with GTPase buffer, Δ PRD-dynamin was added to give a final
 369 concentration of 0.22 mg/ml, incubated for 30 min and then rinsed again with GTPase
 370 buffer before imaging.

371 **High-Speed atomic force microscopy (HS-AFM) images.** A HS-AFM SS-NEX (RIBM,
 372 Japan) (27) setup was equipped with short (7 μ m long and 2 μ m large) cantilevers with
 373 nominal spring constant of 150 pN nm⁻¹, resonance frequency of about 600 kHz and a
 374 quality factor $Q = 1.5$ in liquid (Nanoworld), was used for movie acquisition. The
 375 microscope was operated in amplitude modulation mode, where the cantilever oscillates
 376 at a frequency close to its resonance frequency. The phase-shift in the oscillation of the
 377 cantilever is used to create the phase images, which provide information about the
 378 viscoelastic properties of the material. Herein, both topographic and phase images are
 379 reported. Either bare mica or mica covered by DPPC:Biotinyl CAP PE, 9:1, mol:mol, SLBs
 380 were used as support, in the latest followed by the addition of 0.1 μ M streptavidin.
 381 Streptavidin was incubated for 5 min and rinsed 10 times with GTPase buffer. Finally,
 382 the dynamin-DOPS tubule sample was added and incubated for 30 min at RT. During
 383 imaging, GTP, GDP \cdot AlF₄⁻ or GMP-PCP solutions were added directly to the HS-AFM fluid
 384 cell, if indicated. HS-AFM movies were analyzed in ImageJ, self-written analysis routines
 385 and WSxM 5.0 software (Nanotec (28)).

386 **Quantitative nanomechanical mapping.** The AFM fluid cell contained 100 μ L of GTP
 387 buffer. After imaging in the absence of GTP, GTP solution was added through the inlet of
 388 the AFM fluid cell to give a final concentration of ~ 2.5 mM.

389 Nanomechanical measurements were performed on a Nanoscope-V AFM (Bruker, Santa
 390 Barbara, CA, USA) equipped with Nanoscope-8 control software, in Peak-Force
 391 Quantitative-Nanomechanics (PF-AFM) mode. We used Si₃N₄ cantilevers with a nominal
 392 spring constant of 150 pN nm⁻¹ and silicon tips with a nominal radius of 2 nm (MSNL,
 393 Bruker, Santa Barbara, CA, USA). The actual spring constant of the cantilever was
 394 determined using the thermal fluctuation method (29). Images were obtained at a
 395 resolution of 512 by 512 pixels at a line scan rate of 1 Hz. In PF-AFM, the sample support
 396 is oscillated at a constant rate (2 kHz) and amplitude (15 nm). Monitoring the cantilever
 397 deflection in each oscillation cycle allows to obtain a force-distance curve on each pixel
 398 of the image. The approach trace was used to control the maximum force applied
 399 (~ 300 pN). The retract trace was used to determine the Young's modulus by fitting the
 400 Hertz model of a spherical tip of radius R indenting an elastic half-space:

$$401 \quad F = \frac{4E}{3(1-\nu^2)} \sqrt{R} \delta^{3/2}, \quad (\text{equation 1})$$

402 where F is the force applied, ν is the Poisson ratio (assumed 0.5 as for a perfectly elastic
 403 uncompressed material) and δ the indentation. The tip radius was assumed 2 nm, its
 404 nominal radius. To avoid contributions from long-range electrostatic forces and short-

405 range van der Waals interactions, the Hertz model fit was restricted to a range between
 406 30% and 90% of the maximum F. Image and data processing was performed using
 407 Gwyddion 2.38 open software (gwyddion.net).

408 **Acknowledgements:**

409 The authors would like to thank Oliver Daumke, Pierre-Emmanuel Milhiet, Peter
 410 Hinterdorfer for their appreciable comments on the manuscript. The Scheuring group
 411 acknowledges funding support from: ANR grants, ANR-Nano ANR-12-BS10-009-01 and
 412 ANR-BBMS ANR-12-BSV8-0006-01, and a European Research Council (ERC) starting
 413 (consolidator) grant #310080-MEM-STRUCT-AFM. The Roux group acknowledges
 414 funding support from: Human Frontier Science Program (HFSP), Young Investigator
 415 Grant #RGY0076-2008: the European Research Council (ERC), starting (consolidator)
 416 grant #311536-MEMFIS: the Swiss National Fund for Research, grants
 417 #131003A_130520 and #131003A_149975.

418

419 **References:**

- 420 1. Ferguson SM & De Camilli P (2012) Dynamin, a membrane-remodelling GTPase.
 421 *Nat Rev Mol Cell Biol* 13(2):75-88.
- 422 2. Sweitzer SM & Hinshaw JE (1998) Dynamin undergoes a GTP-dependent
 423 conformational change causing vesiculation. *Cell* 93(6):1021-1029.
- 424 3. Danino D, Moon KH, & Hinshaw JE (2004) Rapid constriction of lipid bilayers by
 425 the mechanochemical enzyme dynamin. *J Struct Biol* 147(3):259-267.
- 426 4. Sundborger AC, *et al.* (2014) A dynamin mutant defines a superconstricted
 427 pre-fission state. *Cell reports* 8(3):734-742.
- 428 5. Faelber K, *et al.* (2011) Crystal structure of nucleotide-free dynamin. *Nature*
 429 477(7366):556-560.
- 430 6. Ford MG, Jenni S, & Nunnari J (2011) The crystal structure of dynamin. *Nature*
 431 477(7366):561-566.
- 432 7. Reubold TF, *et al.* (2015) Crystal structure of the dynamin tetramer. *Nature*
 433 525(7569):404-8.
- 434 8. Chappie JS, Acharya S, Leonard M, Schmid SL, & Dyda F (2010) G domain
 435 dimerization controls dynamin's assembly-stimulated GTPase activity. *Nature*
 436 465(7297):435-440.
- 437 9. Gao S, *et al.* (2010) Structural basis of oligomerization in the stalk region of
 438 dynamin-like MxA. *Nature* 465(7297):502-506.
- 439 10. Chen Y, Zhang P, Egelman E, & Hinshaw JE (2004) The stalk region of dynamin
 440 drives the constriction of dynamin tubes. *Nat Struct Mol Biol* v11(n6):574-575.
- 441 11. Zhang P & Hinshaw JE (2001) Three-dimensional reconstruction of dynamin in
 442 the constricted state. *Nat Cell Biol* 3(10):922-926.
- 443 12. Mears JA, Ray P, & Hinshaw JE (2007) A corkscrew model for dynamin
 444 constriction. *Structure* 15(10):1190-1202.
- 445 13. Chappie JS, *et al.* (2011) A pseudoatomic model of the dynamin polymer
 446 identifies a hydrolysis-dependent powerstroke. *Cell* 147(1):209-222.
- 447 14. Roux A, Uyhazi K, Frost A, & De Camilli P (2006) GTP-dependent twisting of
 448 dynamin implicates constriction and tension in membrane fission. *Nature*
 449 441(7092):528-531.

- 450 15. Morlot S, Lenz M, Prost J, Joanny JF, & Roux A (2010) Deformation of dynamin
451 helices damped by membrane friction. *Biophys J* 99(11):3580-3588.
- 452 16. Ando T, Uchihashi T, & Scheuring S (2014) Filming Biomolecular Processes by
453 High-Speed Atomic Force Microscopy. *Chemical Reviews* 114(6):3120-3188.
- 454 17. Chiaruttini N, *et al.* (2015) Relaxation of Loaded ESCRT-III Spiral Springs Drives
455 Membrane Deformation. *Cell* 163(4):866-879.
- 456 18. Kodera N, Yamamoto D, Ishikawa R, & Ando T (2010) Video imaging of walking
457 myosin V by high-speed atomic force microscopy. *Nature* 468(7320):72-76.
- 458 19. Takei K, Slepnev VI, Haucke V, & De Camilli P (1999) Functional partnership
459 between amphiphysin and dynamin in clathrin-mediated endocytosis. *Nat Cell*
460 *Biol* 1(1):33-39.
- 461 20. Morlot S, *et al.* (2012) Membrane shape at the edge of the dynamin helix sets
462 location and duration of the fission reaction. *Cell* 151(3):619-629.
- 463 21. Colom A, Casuso I, Rico F, & Scheuring S (2013) A hybrid high-speed atomic
464 force-optical microscope for visualizing single membrane proteins on eukaryotic
465 cells. *Nat Commun* 4:2155.
- 466 22. Stowell MH, Marks B, Wigge P, & McMahon HT (1999) Nucleotide-dependent
467 conformational changes in dynamin: evidence for a mechanochemical molecular
468 spring. *Nat Cell Biol* 1(1):27-32.
- 469 23. Marks B, *et al.* (2001) GTPase activity of dynamin and resulting conformation
470 change are essential for endocytosis. *Nature* 410(6825):231-235.
- 471 24. Antony B, *et al.* (2016) Membrane fission by dynamin: what we know and what
472 we need to know. *EMBO J* 35(21):2270-2284.
- 473 25. Morlot S & Roux A (2013) Mechanics of dynamin-mediated membrane fission.
474 *Annual review of biophysics* 42:629-649.
- 475 26. Roux A (2014) Reaching a consensus on the mechanism of dynamin? *F1000prime*
476 *reports* 6:86.
- 477 27. Ando T, *et al.* (2001) A high-speed atomic force microscope for studying
478 biological macromolecules. *Proc Natl Acad Sci U.S.A* 98(22):12468-72.
- 479 28. Horcas I, *et al.* (2007) WSXM: A software for scanning probe microscopy and a
480 tool for nanotechnology. *Review of Scientific Instruments* 78(1).
- 481 29. Hutter JL & Bechhoefer J (1993) Calibration of atomic-force microscope tips.
482 *Review of Scientific Instruments* 64(7):1868-1873.
483

484 **Figures legends:**

485 **Fig. 1) HS-AFM imaging of dynamin-coated tubules. a)** Two proposed models of
 486 dynamin constriction. Top left: basic structural features of the dynamin dimer and of the
 487 tetramer: blue and orange GTPase domains from 2 adjacent dynamin dimers form the
 488 “helical dimer”, a visible unit in the helical form. Bottom left: helix assembly of the
 489 dimers. Bottom right: compaction model (schematic but not precise representation of
 490 dimer conformational changes, see (12) for details). Top right: Torsion model: The
 491 relative movement of helix turns is highlighted by the relative displacement of the blue-
 492 yellow dimers interacting in the non-constricted state. **b)** DOPS tubule with polymerized
 493 Δ PRD-dynamin before GTP-addition. **c)** Image sequence during GTP-hydrolysis of the
 494 area outline by dashed rectangle in b) and d). 0s is the time of GTP-injection. White
 495 arrowheads point at a constriction site. Orange arrowheads point at a fission site. **d)**
 496 Δ PRD-dynamin-DOPS tubule shown in b), after GTP-addition.

497

498 **Fig. 2) Constriction and fission of dynamin-coated tubules observed by HS-AFM. a)**
 499 Image sequence of Δ PRD-dynamin-coated tubules, adsorbed on a mica-supported
 500 bilayer (see Supplementary Methods). During the experiment, GTP was injected twice,
 501 and the dynamin helix conformational change monitored as a function of time. White
 502 arrowheads point at constriction sites, orange arrowhead at fission sites. **b)** Another
 503 example similar to a), with three consecutive GTP-injections. White arrowheads point at
 504 a constriction site, which later became fission sites (indicated by F.P.1 (fission point 1)
 505 and F.P.2 (fission point 2)). **c)** Kymograph along the dashed line F.P.1 in b). Red dashed
 506 lines indicate GTP-additions. **d)** Helix profile kymograph along the long tubule axis
 507 (dashed line labeled ‘d’ in image b), crossing F.P.2) revealing morphological changes of
 508 the dynamin helix. Arrows point at turn height reduction consistent with constriction
 509 (white), lateral separation of adjacent turns (green), collapse of two turns in one (red),
 510 turn enlargement (blue), and fission (yellow). **e)** Kymograph along the axis of a tubule
 511 not treated with GTP. **f)** Maximum height of F.P.1 and F.P.2 as a function of time in b). **g)**
 512 Height profile along the dashed line at F.P.1 in b) before GTP-addition and after the third
 513 GTP-addition. **h)** Maximum height of a tubule not treated with GTP as a function of time.
 514 **i)** Distribution of dynamin helix pitch distances before GTP-addition (grey bars,
 515 19.2 ± 3.6 nm; mean \pm SD, $N=4$) and after GTP-addition (red bars, 15.2 ± 4.9 nm;
 516 mean \pm SD, $N=2$). **j)** Height profiles of the dynamin helix along the tubule axis shown in
 517 Fig. 2B before (grey) and after (red) GTP-addition. **k)** Dynamin helix turn angle (with
 518 respect to the long tubule axis) before (grey) and after (red) GTP-addition (from movies
 519 shown in panels a and b, and another tubule).

520

521 **Fig. 3) GTP-induced turn pairing observed on lipid nanorods. a)** Molecular
 522 interactions between dynamin turns within the helix (yellow arrow) are resolved on a
 523 lipid nanorod. **b)** Distribution of the dynamin helix pitches on lipid nanorods before
 524 (grey bars, 15.4 ± 2.9 nm; mean \pm SD, $N=4$) and after (red bars, 10.8 ± 3.1 nm, $N=4$) GTP-

525 addition. **c)** Dynamin helix images before (left) and after (right) GTP- showing a
526 reduction of the helix pitch, with respective height profiles along the dotted lines
527 (middle). Orange arrowhead point the lipid and white arrowhead dynamin polymerized.
528 **d)** Dynamin helix images before (left) and after (right) GTP-addition showing an
529 increase of the pitch, with respective height profiles along the dotted lines (middle).

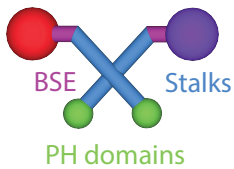
530

531 **Fig. 4) Dynamin helix turns relative displacements during constriction. a)** Time-
532 lapse sequence of zipper-like dissociation-association movements between neighboring
533 Δ PRD-dynamin helix turns during GTP-hydrolysis. **b)** Time-lapse images and profile
534 analysis of three Δ PRD-dynamin turns close to a fission site (F:P.2 in Fig. 2) on a DOPS
535 tubule: positions of peaks in each turn are sequentially aligned and misaligned. Colors in
536 lower panels correspond to height profiles of the same color. **c)** Transmission electron
537 microscopy images of dynamin polymerized on stacked supported lipid bilayers before
538 (left) and after (right) GTP-addition. **d)** Kymograph (left, along the red dashed line in
539 image +58s) illustrating the relative movement of Δ PRD-dynamin oligomers on stacked
540 planar membranes. Image sequence (right) displaying the morphological changes of the
541 Δ PRD-dynamin coat on the supported lipid bilayer.

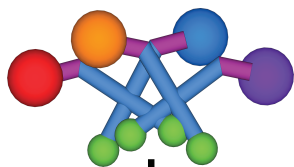
Fig. 1

A Dynammin dimer

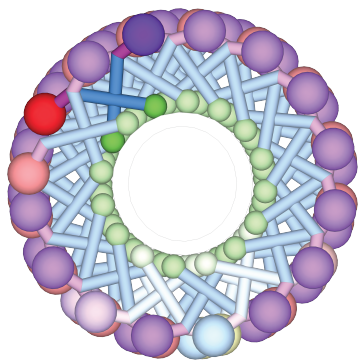
GTPase domain GTPase domain



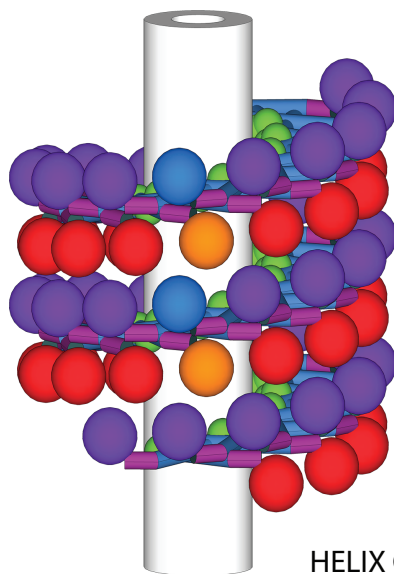
tetramer



assembly



HELIX TORSION



HELIX COMPACTION

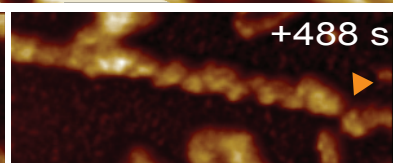
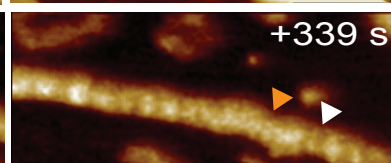
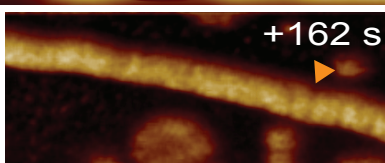
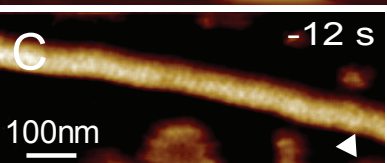
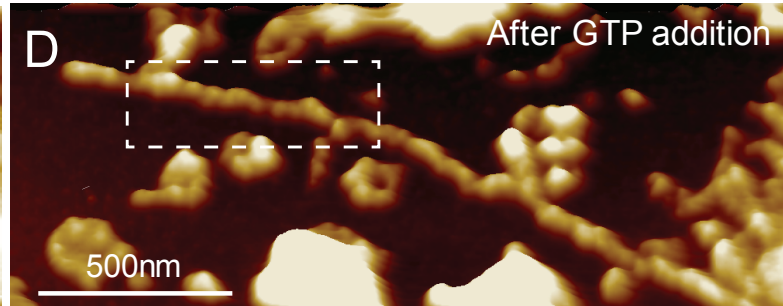
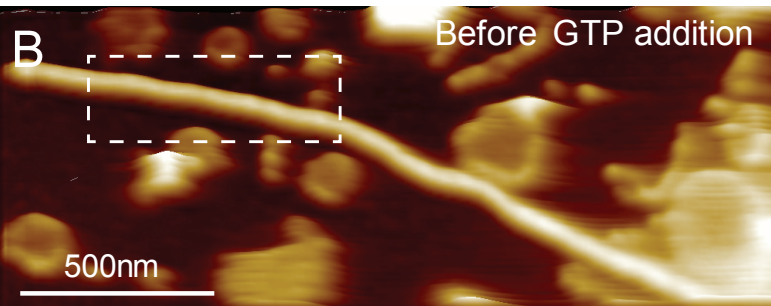
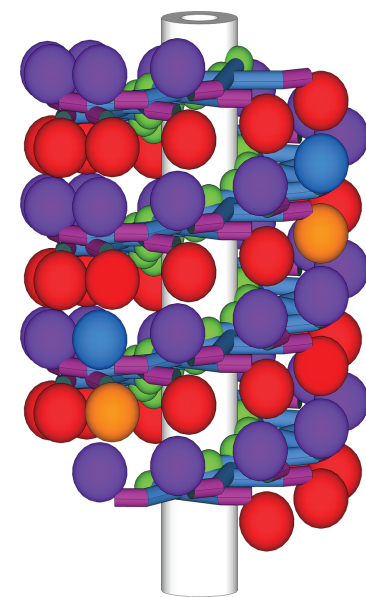
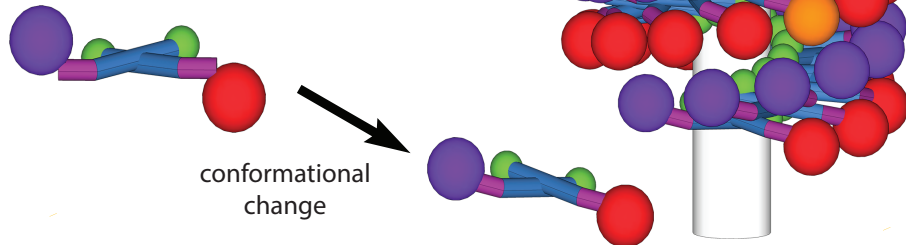


Fig. 2

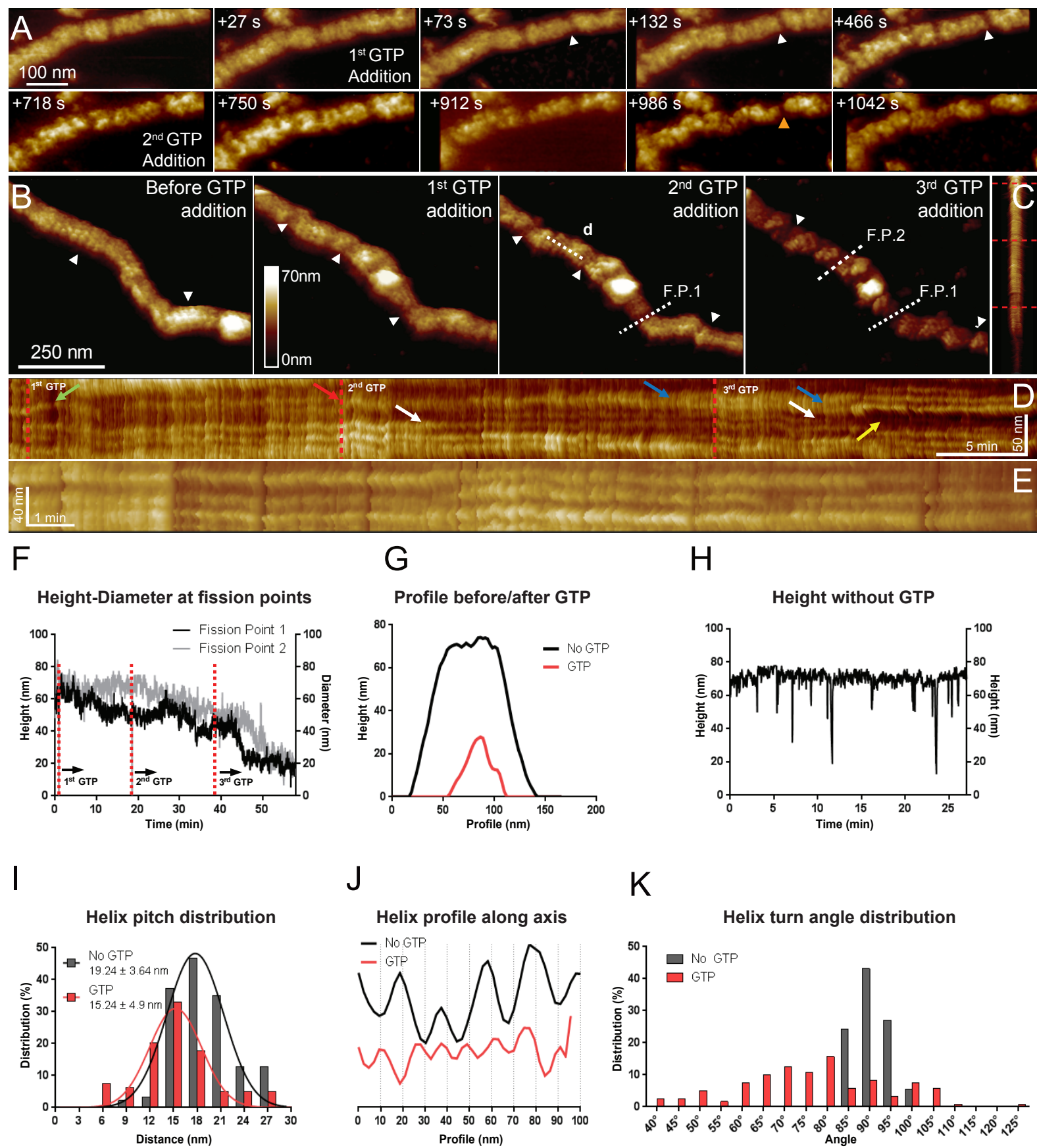


Fig. 3

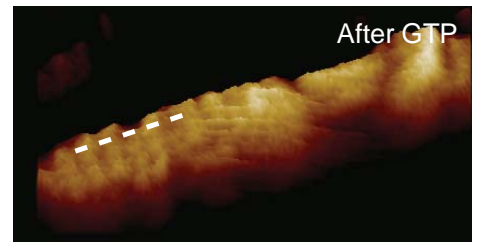
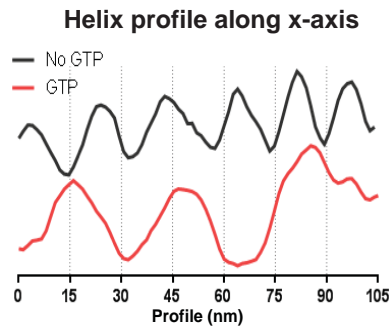
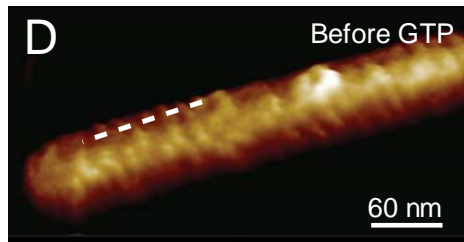
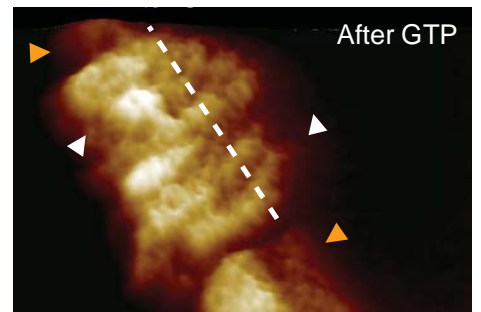
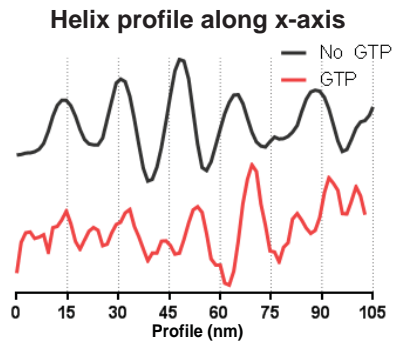
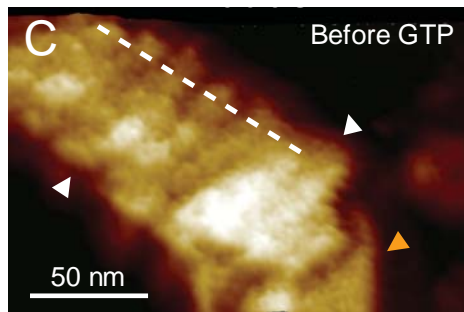
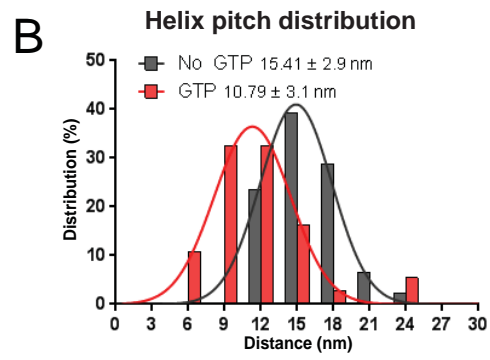
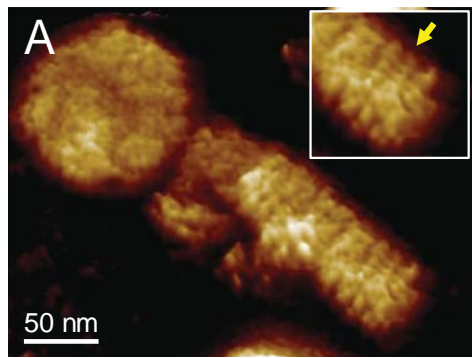


Fig. 4

